Density matrix renormalization group study of nematicity in two dimensions: Application to a spin-1 bilinear-biquadratic model on the square lattice

Wen-Jun Hu,[1] Shou-Shu Gong,[2,*] Hsin-Hua Lai,[3] Qimiao Si,[3,†] and Elbio Dagotto[1,4,‡]
[1]*Department of Physics and Astronomy, University of Tennessee, Knoxville, Tennessee 37996, USA*
[2]*Department of Physics, Beihang University, Beijing 100191, China*
[3]*Department of Physics and Astronomy and Rice Center for Quantum Materials, Rice University, Houston, Texas 77005, USA*
[4]*Materials Science and Technology Division, Oak Ridge National Laboratory, Oak Ridge, Tennessee 37831, USA*

(Received 1 November 2019; revised manuscript received 22 December 2019; published 15 January 2020)

Nematic order is an exotic property observed in several strongly correlated systems, such as iron-based superconductors. Using large-scale density matrix renormalization group (DMRG) techniques, we study at zero temperature the nematic spin liquid that competes with spin dipolar and quadrupolar orders. We use these nematic orders to characterize different quantum phases and quantum phase transitions. More specifically, we study a spin-1 bilinear-biquadratic Heisenberg model on the square lattice with couplings beyond nearest neighbors. We focus on parameter regions around the highly symmetric $SU(3)$ point where the bilinear and biquadratic interactions are equal. With growing further-neighbor biquadratic interactions, we identify different spin dipolar and quadrupolar orders. We find that the DMRG results for cylindrical geometries correctly detect nematicity in different quantum states and accurately characterize the quantum phase transitions among them. Therefore, spin-driven nematicity, here defined as the spontaneous breaking of the lattice invariance under a 90° rotation, is an order parameter which can be studied directly in DMRG calculations in two dimensions in different quantum states.

DOI: 10.1103/PhysRevB.101.014421

I. INTRODUCTION

Rotational invariance is one of the fundamental lattice symmetries in condensed-matter crystals. The spontaneous breaking of this rotational symmetry can occur via the emergence of magnetic nematicity, which may lead to novel phases. Nematic phases also occur in liquid crystals. In recent years, nematicity has also been found in strongly correlated electronic systems, including the fractional quantum Hall effect [1–9] and iron-based superconductors [10–21]. In such systems, nematicity is usually observed to be accompanied by novel quantum states or new collective excitations, such as the nematic phase without long-range spin order in the iron-based superconductor [20] and the emergent new plasmon excitations in the fractional quantum Hall state [9]. Therefore, studying the origin of nematicity and its interplay with other properties in strongly correlated systems is important not only for understanding the novel states but also for predicting new quantum phases.

Very recently, nematicity was also found at zero temperature in a quantum spin liquid phase with spontaneous lattice C_4 rotational symmetry breaking [22]. This nematic spin liquid was identified in a spin-1 model on the square lattice with bilinear-biquadratic interactions, which is defined as

$$H = \sum_{i,j} J_{ij}\mathbf{S}_i \cdot \mathbf{S}_j + K_{ij}(\mathbf{S}_i \cdot \mathbf{S}_j)^2, \tag{1}$$

where $\mathbf{S}_i$ is a spin-1 operator at site i and J_{ij} and K_{ij} are the bilinear and biquadratic interactions, respectively [23]. Similar bilinear-biquadratic models were studied to describe spin-1 magnetic systems, such as the triangular-lattice layered materials $NiGa_2S_4$ [24] and $Ba_3NiSb_2O_9$ [25,26], the honeycomb-lattice 6HB-$Ba_3NiSb_2O_9$ [27], and the iron pnictide [28] and iron chalcogenide superconductors [29–32]. Thus, such a spin-1 bilinear-biquadratic Hamiltonian is a prototypical model to search for novel quantum phases in frustrated spin-1 systems [33–42].

In one dimension, the ground-state phase diagram of Eq. (1) with nearest-neighbor couplings has been well established [40]. A symmetry-protected topological phase has been identified, known as the Haldane state, with a finite bulk gap and gapless edge states if open boundaries are used [33,43]. In two dimensions, according to the Lieb-Schultz-Mattis-Hastings theorem [44,45], the ground state of such a spin-1 model could be either a conventional ordered state with spontaneous symmetry breaking, a gapless spin liquid, a gapped spin liquid with topological order, or a quantum paramagnet with a unique ground state and finite bulk gap.

With these many fruitful possibilities, studies of novel quantum phases in such two-dimensional systems have attracted much attention, especially near the highly symmetric $SU(3)$ point with equal bilinear and biquadratic interactions $J_{ij} = K_{ij}$ [42,46–55], which has enhanced frustration due to

*shoushu.gong@buaa.edu.cn
†qmsi@rice.edu
‡edagotto@utk.edu

 ©2020 American Physical Society

the strong competition between the two types of interactions. By considering only the nearest-neighbor couplings, a three-sublattice magnetic order has been reported near the $SU(3)$ point on the triangular [47,50,55] and square lattices [42,48–50,54]. Alternatively, the valence bond solid states, which spontaneously break lattice symmetries, including a trimerized ground state on the kagome lattice [46,52] and a plaquette state on the honeycomb lattice [51,53], have also been suggested to exist near the $SU(3)$ point. Most surprisingly, recent large-scale density matrix renormalization group (DMRG) calculations confirmed the three-sublattice order in the triangular $SU(3)$ model but found new evidence to support a nematic quantum spin liquid rather than the three-sublattice magnetic order in the square $SU(3)$ model [22]. This nematic spin liquid is particularly interesting since it does not have either spin dipolar or quadrupolar long-range order but has a nonzero nematic order with C_4 lattice rotational symmetry that is broken while it preserves translational symmetry [22].

Nematicity has rarely been reported in quantum spin liquid states, and its driving force in this setting is still to be understood. In Ref. [22], the nematicity in the spin liquid phase was argued to be caused by the fluctuations peaked at the momentum $(\pi, 2\pi/3)$ on a finite-size cluster. These dominant fluctuations appear clearly in the spin and quadrupolar static structure factors and are proposed to be the result of melting order at momentum $(\pi, 2\pi/3)$. Note that the state with wave vector $(2\pi/3, \pi)$ in a two-dimensional system is totally equivalent: starting from high temperature and cooling down via an annealing or Monte Carlo process, if it were possible, both states have equal chance, similar to the $(\pi, 0)$ and $(0, \pi)$ states in undoped iron superconductors. The cylindrical boundary conditions used here may introduce a small symmetry-breaking preference for $(\pi, 2\pi/3)$, like a small magnetic field up favors, in a ferromagnetic Ising model, the state with all spins up. But these are minor details that do not affect our nematic analysis: there are two quasidegenerate wave vector states, and only one can become the ground state.

The tendency towards $(\pi, 2\pi/3)$ fluctuations can also be discussed using a coupled-chain picture of a conjectured gapless spin liquid; here $2\pi/3$ is twice the parton "Fermi wave vector" for an $SU(3)$ chain, which is associated with the $1/3$ filling of those partons, and π simply reflects the interchain coupling that is relevant in the RG sense [22]. However, the precise origin of the nematicity and dominance of wave vectors $(\pi, 2\pi/3)$ or $(2\pi/3, \pi)$ still require further investigation. Before answering these difficult questions, it is important to establish how nematicity is stabilized in different quantum phases and how it behaves at quantum phase transitions.

In this paper, we use large-scale DMRG calculations to address these issues by simulating the model (1) while adding further-neighbor biquadratic interactions. We focus on parameter regions around the $SU(3)$ point with antiferromagnetic $J_1 = K_1 = 1.0$ (J_1 and K_1 are the nearest-neighbor bilinear and biquadratic interactions, respectively). We show that the small nematic spin liquid region reported recently near the $SU(3)$ point with $K_1 = J_1$ [22] can actually be broadened by adding the second-neighbor (K_2) and third-neighbor (K_3) biquadratic interactions. In addition, with further growing biquadratic interaction strengths, different spin dipolar and quadrupolar orders are identified, characterized by specific spin and quadrupolar correlation functions and structure factors. To better describe the nematicity, we study both the B_{1g} and B_{2g} nematic order channels that have been proposed to classify different rotational symmetry breakings on the square lattice [56].

Through our extensive DMRG simulations, a plethora of new quantum phases are unveiled here, including quantum phases with either B_{1g} or B_{2g} nematicity, as well as phases that preserve lattice rotational symmetry. We find that the obtained nematic orders faithfully describe the quantum states and the corresponding quantum phase transitions. Interestingly, although our DMRG simulations are performed on cylindrical geometries, which *a priori* explicitly break lattice rotational invariance, we show that this explicit breaking leads to small effects for the systems we study. On the other hand, when nematic order parameters are studied in regions where nematicity appears stable, the signal is very robust, much larger than the small effect caused by the geometry. As a consequence, DMRG studies using cylinders can be used to identify quantum phase transitions involving nematicity in addition to the standard analysis of the spin-spin and quadrupolar-quadrupolar correlation functions. Our work thus provides a procedure to use the DMRG to analyze nematic orders and nematic phase transitions in spin square-lattice models, which can be generalized to other geometries.

Our paper is organized as follow. In Sec. II, we introduce computational details and define the order parameters that we will measure. In Secs. III and IV, we show the quantum phase diagrams of model (1) varying K_2 or K_3, and we characterize different spin dipolar and quadrupolar phases by their correlation functions and order parameters. In Sec. V, we calculate nematic orders for different phases and use these nematic orders to characterize the quantum phase transitions. A summary and discussion are given in Sec. VI.

II. METHOD AND ORDER PARAMETERS

In the $SU(2)$ DMRG simulation [57,58], we set the nearest-neighbor (NN) bilinear coupling $J_1 = 1.0$ as the energy scale, and we focus on the parameter regions around the $SU(3)$ point with $K_1 = J_1$. We will consider additional second-neighbor (K_2) or third-neighbor (K_3) biquadratic interactions (see Fig. 1) to study the quantum phases of the system (1) on the square lattice. By adding extra couplings we can enhance the region of stability of the spin liquid found at the SU(3) point, rendering its properties clearer. To reduce the influence of finite-size effects as much as possible, we study the system using both the rectangular cylinder (RC) and the 45°-tilted cylindrical (TC) geometries. These two cylindrical geometries have periodic boundary conditions in the y direction (circumference direction) and open boundaries in the x direction (axis direction), and we denote them as RCL_y and TCL_y (L_y is the number of sites along the short-circumference direction). With regard to the "long" direction along the axis, we analyzed systems with $L_x = 24$ and 36 to confirm that we obtain similar results. Most of our DMRG simulations have focused on the RC6 geometry, which can harbor both three- and two-sublattice order structures. Also, we selected

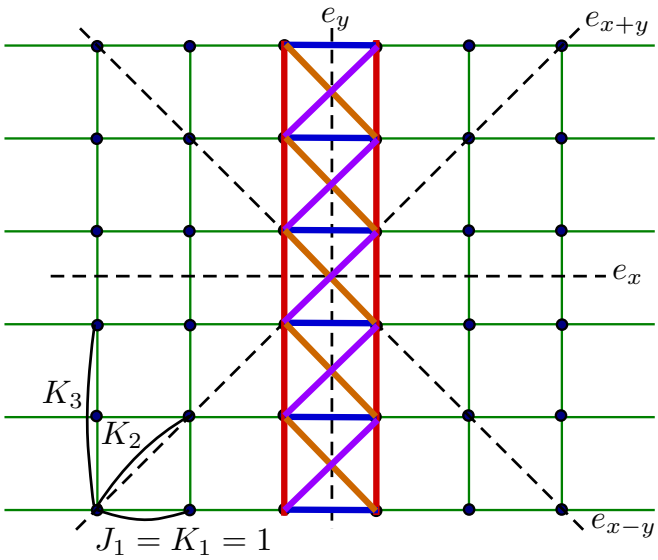

FIG. 1. Sketch illustrating bonds in the middle of the RC6 cylinder used for calculating the nematic order parameters in both the B_{1g} and B_{2g} channels. The dashed lines represent mirror symmetries along e_x, e_y, e_{x+y}, and e_{x-y}. The blue, red, purple, and orange lines represent bonds along the e_x, e_y, e_{x+y}, and e_{x-y} directions, respectively.

some typical points to perform DMRG simulations on RC9 clusters (because they are highly demanding of computer time) to check the stability of the several quantum phases on larger clusters. For three-sublattice orders, we also study the TC geometry for cross-checking purposes. By keeping up to 4000 $SU(2)$ DMRG states, most of the truncation errors in the important intermediate coupling region are about 10^{-7}, while the largest ones in our calculations are around 10^{-5}.

To characterize different quantum states, we calculate spin $\langle \mathbf{S}_i \cdot \mathbf{S}_j \rangle$ and quadrupolar $\langle \mathbf{Q}_i \cdot \mathbf{Q}_j \rangle$ correlation functions as well as their structure factors, where the quadrupolar tensor operator is $\mathbf{Q}_i = (\frac{1}{2}(Q_i^{xx} - Q_i^{yy}), \frac{1}{2\sqrt{3}}(2Q_i^{zz} - Q_i^{xx} - Q_i^{yy}), Q_i^{xy}, Q_i^{yz}, Q_i^{xz})$ [48,59], with $Q_i^{\alpha\beta} = S_i^{\alpha} S_i^{\beta} + S_i^{\beta} S_i^{\alpha} - \frac{4}{3}\delta_{\alpha\beta}$ ($\alpha, \beta = x, y, z$). The quadrupolar correlation function can be expressed as $\mathbf{Q}_i \cdot \mathbf{Q}_j = 2(\mathbf{S}_i \cdot \mathbf{S}_j)^2 + \mathbf{S}_i \cdot \mathbf{S}_j - 8/3$. We perform the Fourier transformation for the correlation functions to obtain the spin structure factor as

$$m_S^2(\mathbf{q}) = \frac{1}{N_s^2} \sum_{i,j} \langle \mathbf{S}_i \cdot \mathbf{S}_j \rangle e^{i\mathbf{q}\cdot(\mathbf{r}_i - \mathbf{r}_j)} \tag{2}$$

and the quadrupolar structure factor as

$$m_Q^2(\mathbf{q}) = \frac{1}{N_s^2} \sum_{i,j} \langle \mathbf{Q}_i \cdot \mathbf{Q}_j \rangle e^{i\mathbf{q}\cdot(\mathbf{r}_i - \mathbf{r}_j)}, \tag{3}$$

where sites i, j are chosen inside the middle region of size $N_s = L_y \times 2L_y$ in order to avoid the effects of open edges and also to be able to consider both two- and three-sublattice orders [22]. We use these correlation functions and structure factors to detect spin dipolar and quadrupolar orders. As the range of accessible system sizes available for DMRG spin-1 systems is limited due to the difficulty of the calculation,

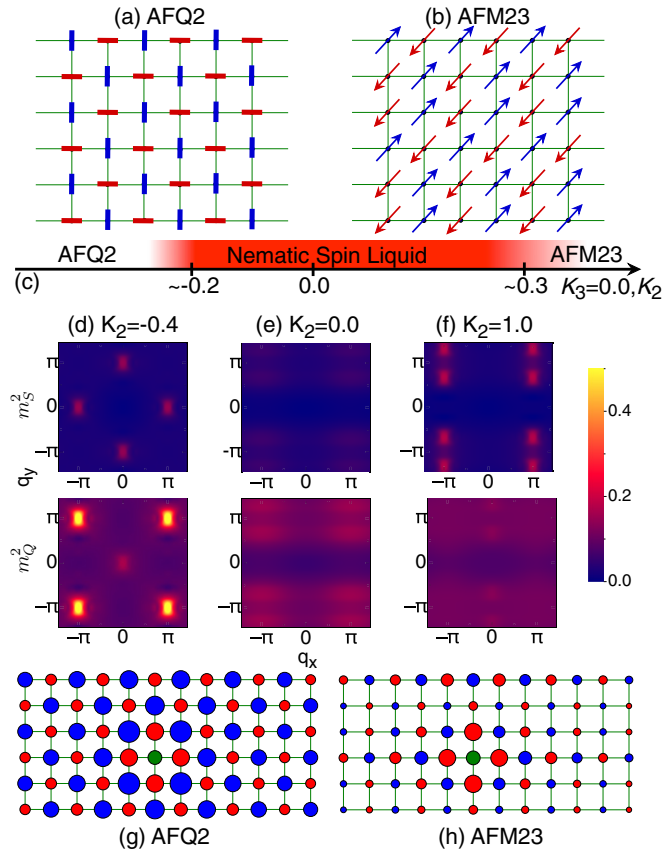

FIG. 2. Quantum phase diagram of the $SU(3)$ model with additional K_2 interaction at $K_3 = 0$. (a) and (b) Sketches illustrating the AFQ2 and AFM23 orders. (c) Quantum phase diagram of the spin-1 $SU(3)$ Heisenberg model on the square lattice with $J_1 = K_1 = 1.0$, $K_3 = 0$, and varying K_2. The regime of the nematic spin liquid around the $SU(3)$ point is indicated by red shading. (d)–(f) Spin (m_S^2) and quadrupolar (m_Q^2) structure factors for different values of K_2, which are obtained from the middle 6×12 site region of a long RC6 cylinder. The top and bottom panels are for m_S^2 and m_Q^2, respectively. (g) The real-space quadrupolar correlation functions for the AFQ2 state with $K_2 = -0.4$ in the middle of the RC6 cylinder. (h) The real-space spin correlation functions for the AFM23 state with $K_2 = 1.0$ in the middle of the RC6 cylinder. The green site is the reference site; blue and red denote positive and negative correlations of the sites with respect to the reference site, respectively. The areas of circles are proportional to the magnitude of the correlations.

we cannot perform detailed finite-size scaling analysis. Fortunately, in our studied parameter regions the measured spin dipolar and quadrupolar orders are strong, and for this reason they can be clearly identified on the $L_y = 6, 9$ finite systems we employ.

In some of the magnetic order phases we investigated, the lattice rotational symmetry of 90° is also broken (nematicity), accompanied by spin rotational symmetry breaking. To study better this nematicity, we define the lattice nematic order parameters in both the B_{1g} and B_{2g} channels for both spin dipolar and quadrupolar operators [22,29,56,60], as shown in Fig. 1. Therefore, we have four nematic order parameters, with two of them in the B_{1g} channel for the NN

bonds as

$$\sigma^{S}_{B1g} = \frac{1}{N_m}\sum_i [\langle \mathbf{S}_i \cdot \mathbf{S}_{i+\hat{x}}\rangle - \langle \mathbf{S}_i \cdot \mathbf{S}_{i+\hat{y}}\rangle], \quad (4)$$

$$\sigma^{Q}_{B1g} = \frac{1}{N_m}\sum_i [\langle \mathbf{Q}_i \cdot \mathbf{Q}_{i+\hat{x}}\rangle - \langle \mathbf{Q}_i \cdot \mathbf{Q}_{i+\hat{y}}\rangle] \quad (5)$$

and the other two parameters in the B_{2g} channel for the next-NN bonds as

$$\sigma^{S}_{B2g} = \frac{1}{N_m}\sum_i [\langle \mathbf{S}_i \cdot \mathbf{S}_{i+\hat{x}+\hat{y}}\rangle - \langle \mathbf{S}_i \cdot \mathbf{S}_{i+\hat{x}-\hat{y}}\rangle], \quad (6)$$

$$\sigma^{Q}_{B2g} = \frac{1}{N_m}\sum_i [\langle \mathbf{Q}_i \cdot \mathbf{Q}_{i+\hat{x}+\hat{y}}\rangle - \langle \mathbf{Q}_i \cdot \mathbf{Q}_{i+\hat{x}-\hat{y}}\rangle], \quad (7)$$

where $\hat{x}$ and $\hat{y}$ denote the unit vectors along the two directions and N_m is the number of sites of the two columns in the middle of the cylinder. Both the nonzero B_{1g} and B_{2g} nematic order parameters characterize a C_4 symmetry breaking on the square lattice, but the two order parameters are related to different mirror symmetries. The B_{1g} order preserves the mirror symmetries along e_x and e_y but breaks the mirror symmetries along e_{x+y} and e_{x-y}. On the other hand, the B_{2g} order preserves the mirror symmetries along e_{x+y} and e_{x-y} but breaks the symmetries along e_x and e_y. In DMRG simulations on cylindrical geometries, lattice C_4 rotational symmetry is naturally broken, and thus, the corresponding nematic order parameter would be nonzero when using finite circumferences. However, for quantum states without C_4 symmetry breaking, the cylinder-induced explicit nonzero nematic order was found to be very small, and it decreases rapidly with growing circumference (see below). For states with intrinsic C_4 symmetry breaking, on the other hand, a robust nematic order parameter was found. As a consequence, this aspect is under control in our study.

For the benefit of the readers, we would like to make two additional comments: (1) we have also performed linear flavor-wave calculations [22,48] to study the same parameter regions as those used for the DMRG simulations. However, due to the spurious divergence of both spin dipolar and quadrupolar order parameters when using this technique, we could not obtain reasonable flavor-wave phase diagrams to report. For this reason, we decided not to discuss such calculations in this publication. (2) Our investigation focuses on finding a robust region of stability of the previously reported nematic spin liquid [22]. But at present we do not know which specific material may display the needed robust values of the biquadratic terms K_1, K_2, and K_3. This matter will be investigated in the near future using more realistic multiorbital Hubbard systems with large on-site coupling U.

III. QUANTUM PHASE DIAGRAM WITH K_2

First, we study the quantum phase diagram of the model while varying K_2 in the absence of K_3, with the resulting phase diagram shown in Fig. 2. We found three phases in this system. In the nematic spin liquid around the $SU(3)$ point [22], both spin and quadrupolar structure factors in Fig. 2(e) have weak peaks at momentum $(\pi, 2\pi/3)$ on the RC6 cylinder. As K_2 decreases down to $K_2 < -0.2$, an antiferroquadrupolar ordered phase with the dominant peak at momentum (π, π) (AFQ2) arises, as shown in Figs. 2(a) and 2(d). The spin structure factor has four weak peaks at momenta $(0, \pm\pi)$ and $(\pm\pi, 0)$. The real-space quadrupolar correlations in Fig. 2(g) clearly show two-sublattice structures in both the x and y directions. With growing $K_2 > 0$, the system transits to an antiferromagnetic order with the dominant peak at $(\pi, 2\pi/3)$ (AFM23) in the spin structure factor, as shown in Figs. 2(b) and 2(f). The real-space spin correlations in Fig. 2(h) also suggest two- and three-sublattice structures along the x and y directions, respectively.

Considering the values of the peaks in both spin and quadrupolar structure factors, we plot the spin (m_S^2) and quadrupolar (m_Q^2) order parameters at different momenta as a function of K_2 in Figs. 3(a) and 3(b). In Fig. 3(a), we find a sharp drop in $m_S^2(0,\pi)/(\pi,0)$ at $K_2 \simeq -0.2$. Meanwhile, $m_Q^2(\pi,\pi)$ also has a sharp drop, which indicates a sharp phase transition between AFQ2 and the nematic spin liquid, likely a first-order transition signaled by a level crossing. For large $K_2 \simeq 1.0$, the dominant order parameter is $m_S^2(\pi, 2\pi/3)$, suggesting the emergence of spin AFM23 order. Both order parameters m_S^2 and m_Q^2 continuously change with growing $K_2 > 0.0$. Due to our limitations in system size, it is not easy to identify the precise transition point between the nematic spin liquid and the AFM23 phase. Thus, in our sketched phase diagram only a diffuse region is shown for the transition.

To characterize the different ordered phases in real space, we plot log-linear figures for both the spin $\langle \mathbf{S}_i \cdot \mathbf{S}_j\rangle$ and quadrupolar $\langle \mathbf{Q}_i \cdot \mathbf{Q}_j\rangle$ correlations on the long RC6 cylinder in Figs. 3(c) and 3(d). Around the $SU(3)$ point, both spin and quadrupolar correlations decay very fast, supporting the previously reported presence of a quantum spin liquid phase in this region [22]. For the AFQ2 phase, the quadrupolar correlation of the blue squares with $K_2 = -0.4$ in Fig. 3(d) clearly shows long-range quadrupolar order. In the spin correlations of Fig. 3(c), we find that the results for the purple upward triangles with $K_2 = 1.0$ strongly suggest long-range magnetic order for the AFM23 phase. Also, we observe that the spin correlations at $K_2 = 0.4$ are enhanced dramatically compared to those for the SU(3) point and $K_2 = 0.2$, which suggests that the AFM23 order develops gradually approximately at $K_2 \sim 0.3$.

IV. QUANTUM PHASE DIAGRAM WITH K_3

We have also investigated the model with $J_1 = K_1 = 1.0$, varying K_3, at $K_2 = 0.0$. As in the previous case, we also obtained a rich quantum phase diagram, as shown in Fig. 4, which now has four quantum phases. Besides the nematic spin liquid around the $SU(3)$ point, we also find three spin dipolar or quadrupolar ordered phases. At the $K_3 > 0.1$ region, the system displays an antiferroquadrupolar order with the ordering peak at momentum $(2\pi/3, 2\pi/3)$ (AFQ3). The real-space quadrupolar correlations in Fig. 4(j) show three-sublattice orders in both the x and y directions. For $K_3 < 0.0$, there are two quantum phase transitions. As K_3 decreases from 0.0, the nematic spin liquid first transits to an antiferromagnetic order with the momentum peak at $(2\pi/3, 2\pi/3)$ (AFM3), which is stable only in the narrow region $-0.3 < K_3 < -0.2$ (the real-space spin configuration of the AFM3

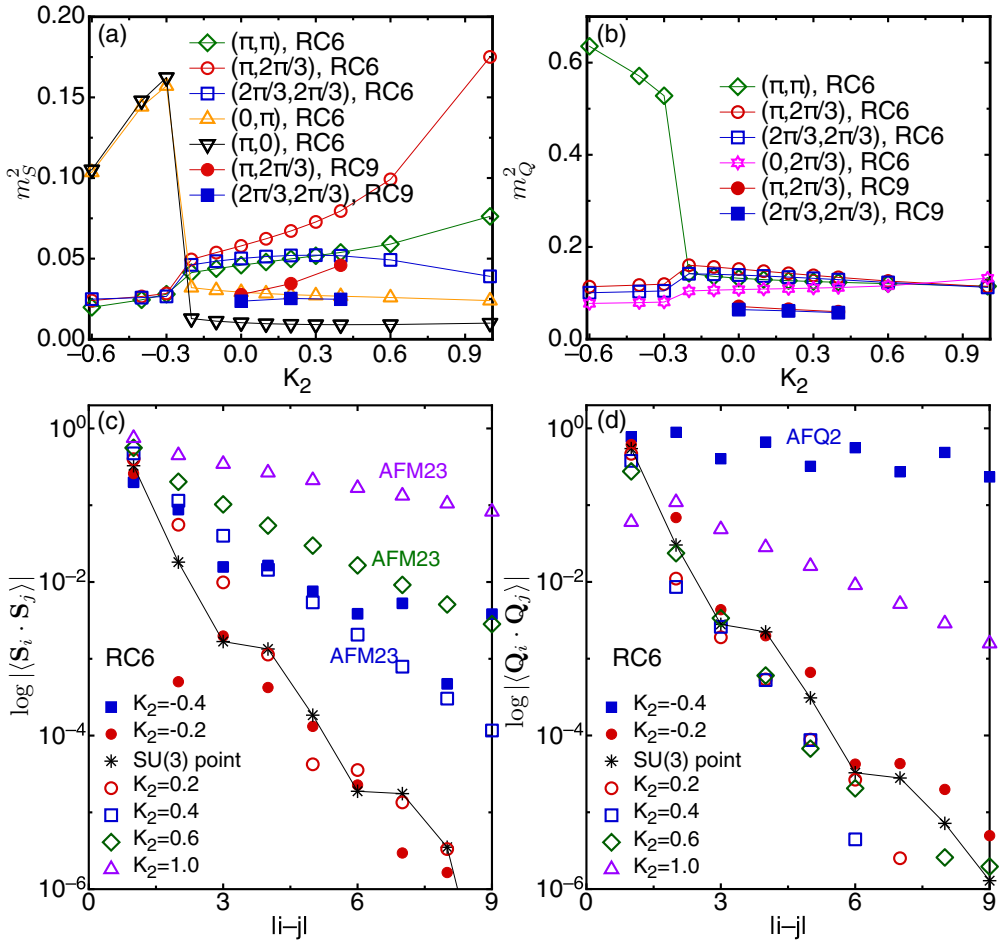

FIG. 3. Interaction dependence of order parameters and correlation functions in the $SU(3)$ model with additional K_2 coupling. (a) and (b) Spin (m_S^2) and quadrupolar (m_Q^2) order parameters for $J_1 = K_1 = 1.0$, $K_3 = 0.0$ at different momenta as a function of K_2 on the RC6 and RC9 cylinders. Both order parameters are obtained from the middle 6×12 sites on the RC6 cylinder or the middle 9×18 sites on the RC9 cylinder. (c) and (d) The log-linear plots of spin $\langle \mathbf{S}_i \cdot \mathbf{S}_j \rangle$ and quadrupolar $\langle \mathbf{Q}_i \cdot \mathbf{Q}_j \rangle$ correlations as a function of the distance on the RC6 cylinder.

is similar to the real-space quadrupolar configuration of the AFQ3). Note that this AFM3 state was suggested to be the ground state of the model at the $SU(3)$ point [42,48–50,54]. Thus, we have the capability to observe this phase if it is stable. However, in our DMRG calculation the $SU(3)$ point realizes a spin liquid state, and the AFM3 state is indeed stable but only in a neighboring region, which implies that the AFM3 state is indeed a very competitive state in the search for the ground state of the $SU(3)$ model. The second phase transition happens at $K_3 \simeq -0.3$, where the system moves into an antiferroquadrupolar phase with the dominant peak at momentum (π, π) and weak peaks at momenta $(\pi, 0)$, $(0, \pi)$, $(0, 0)$ (AFQ4). According to the real-space quadrupolar correlations shown in Fig. 4(i), the unit cell of the AFQ4 state includes four sites.

In Figs. 5(a) and 5(b), we show the spin (m_S^2) and quadrupolar (m_Q^2) order parameters at different momenta as a function of K_3. With growing K_3 starting from $K_3 = -0.6$, the magnetic order parameter $m_S^2(2\pi/3, 2\pi/3)$ has a sharp jump at $K_3 \simeq -0.3$, and there is a sharp drop of the quadrupolar order parameter $m_Q^2(\pi, \pi)$ as well, which indicates a sharp phase transition (first-order level crossing) between the AFQ4 and AFM3 phases. The AFM3 phase exists in a small region, and $m_S^2(2\pi/3, 2\pi/3)$ drops sharply at $K_3 \simeq -0.2$, suggesting again a sharp transition to the nematic spin liquid. The third phase transition happens at $K_3 \simeq 0.1$ between the nematic spin liquid and the AFQ3 phase, which is characterized by an increasing $m_Q^2(2\pi/3, 2\pi/3)$.

The spin and quadrupolar order phases are further characterized by spin and quadrupolar correlations in the long RC6 cylinder, as shown in Figs. 5(c) and 5(d). Although the AFM3 phase region is narrow, the AFM3 order is clearly shown at $K_3 = -0.25$ by the spin correlations that decay quite slowly. A larger region of stability for the AFM3 order might be realized by considering other interactions. For $K_3 = -0.3$ and 0.3, the AFQ4 and AFQ3 orders are supported by strong quadrupolar correlations.

V. NEMATICITY

Since some of the spin dipolar and quadrupolar orders also break lattice rotational symmetry, we now turn to analyzing the nematicity of the different quantum phases by calculating four nematic order parameters in both the B_{1g} and B_{2g} chan-

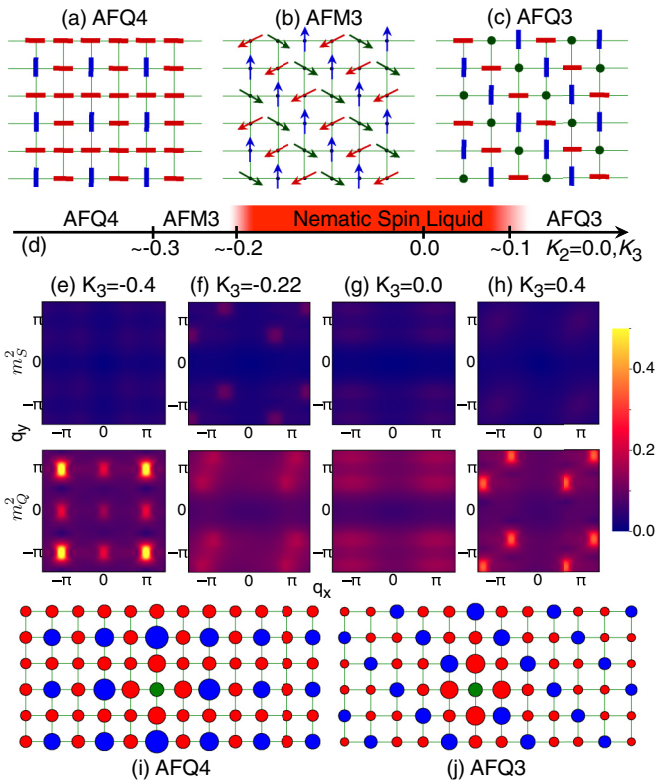

FIG. 4. Quantum phase diagram of the $SU(3)$ model with additional K_3 interaction. (a)–(c) Sketches illustrating the AFQ4, AFM3, and AFQ3 phases, respectively. (d) Quantum phase diagram of the spin-1 $SU(3)$ Heisenberg model on the square lattice with $J_1 = K_1 = 1.0$, $K_2 = 0.0$, and varying K_3. The regime of the nematic spin liquid around the $SU(3)$ point is indicated by red shading. (e)–(h) Spin (m_S^2) and quadrupolar (m_Q^2) structure factors for different values of K_3, which are obtained from the middle 6×12 sites of the RC6 cylinder. The top and bottom panels are for m_S^2 and m_Q^2, respectively. (i) The real-space quadrupolar correlation functions for the AFQ4 state with $K_3 = -0.4$ in the middle of the RC6 cylinder. (j) The real-space quadrupolar correlation functions for the AFQ3 state with $K_3 = 0.4$ in the middle of the RC6 cylinder. The green site is the reference site; blue and red denote positive and negative correlations of the sites with respect to the reference site, respectively. The areas of circles are proportional to the magnitude of correlations.

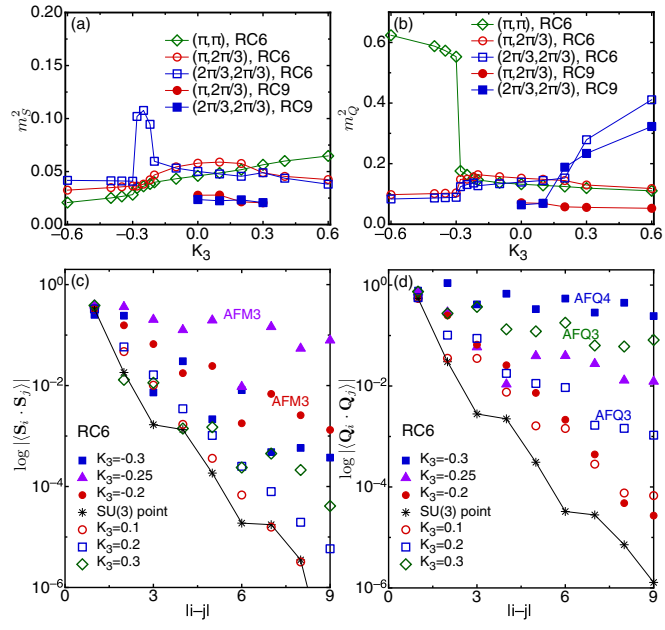

FIG. 5. Interaction dependence of the order parameters and correlation functions in the $SU(3)$ model with additional K_3 coupling. (a) and (b) Spin (m_S^2) and quadrupolar (m_Q^2) order parameters for $J_1 = K_1 = 1.0$, $K_2 = 0.0$ at different momenta vs K_3 on the RC6 and RC9 cylinders. Both order parameters are obtained from the middle 6×12 sites on the RC6 cylinder or the middle 9×18 sites on the RC9 cylinder. (c) and (d) Log-linear plots of the spin $\langle \mathbf{S}_i \cdot \mathbf{S}_j \rangle$ and quadrupolar $\langle \mathbf{Q}_i \cdot \mathbf{Q}_j \rangle$ correlations as a function of the distance on the RC6 cylinder for different values of K_3.

nels for spin ($\sigma^S_{B1g/B2g}$) and quadrupolar ($\sigma^Q_{B1g/B2g}$) operators, as defined in Eqs.(4)–(7). The nematic order parameters for $J_1 = K_1 = 1.0$, $K_3 = 0.0$ as a function of K_2 are shown in Fig. 6(a). In the AFQ2 phase which preserves C_4 symmetry, both the B_{1g} and B_{2g} nematic orders in spin and quadrupolar channels are quite small. The reason the B_{1g} nematicity is not exactly zero (although it is very small) in the AFQ2 regime is the explicit symmetry breaking caused by the cylindrical geometry in this channel (while in the B_{2g} channel the cylinder does not explicitly break the symmetry). The B_{1g} quantities should decay to zero as the width of the cylinder increases in the AFQ2 phase. The results also indicate that the symmetry-breaking effects due to the cylindrical geometry are small. As K_2 increases from negative values, both the B_{1g} nematic order parameters σ^S_{B1g} and σ^Q_{B1g} present a big jump at $K_2 \simeq -0.2$, which is consistent with the sharp phase transition from AFQ2 to the nematic spin liquid with C_4 symmetry breaking discussed before. With further increasing K_2, the B_{2g} nematic orders remain quite small in the spin liquid, but the B_{1g} orders are finite, as recently reported, which indicates that both the nematic spin liquid and the AFM23 states have mirror symmetries along e_x and e_y but break the mirror symmetries along e_{x+y} and e_{x-y}. We wish to remark that in both the nematic spin liquid and the AFM23 phase stabilized at larger K_2, the quadrupolar nematicity in B_{1g} σ^Q_{B1g} is dominant, especially deep in the AFM23 phase such as at $K_2 = 1.0$.

For the case with $J_1 = K_1 = 1.0$, $K_2 = 0.0$, and changing K_3, we show the nematic orders in Fig. 6(b). Like in the AFQ2 phase, both the B_{1g} and B_{2g} nematic orders are small for the AFQ4 phase with C_4 symmetry. With further increasing K_3, we find three sharp changes in the B_{2g} nematic orders at $K_3 \simeq -0.3$, -0.2, and 0.1, which agrees with the three phase transitions shown in Fig. 4. In the AFM3 phase, the B_{2g} nematicity in the spin channel σ^S_{B2g} is dominant, while σ^Q_{B2g} is larger in the AFQ3 phase. The strong B_{2g} nematicity indicates that the AFM3 and AFQ3 orders break the mirror symmetries along e_x and e_y. We noticed that there are small values of σ^S_{B1g} and σ^Q_{B1g} in both the AFM3 and AFQ3 phases, which decay in magnitude from RC6 to RC9 and will likely vanish in the thermodynamic limit. Furthermore, we have performed DMRG simulations for the AFM3 and AFQ3 phases on twisted TC6 cylinders, which are rotated from the RC6 geometry by 45°. In this case we obtain much smaller B_{1g} nematic order parameters, as shown in

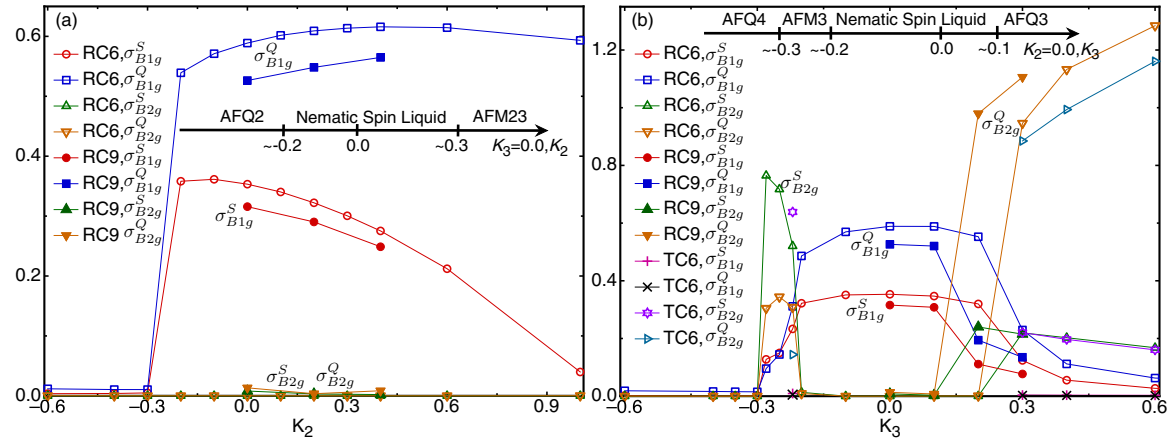

FIG. 6. Nematic order parameters in the B_{1g} (σ^S_{B1g} and σ^Q_{B1g}) and B_{2g} (σ^S_{B2g} and σ^Q_{B2g}) channels (a) vs K_2 at $K_3 = 0$ and (b) vs K_3 at $K_2 = 0$ on the RC6 and RC9 cylinders. The insets show the corresponding quantum phase diagrams.

Fig. 6, which is consistent with our overall description of the results.

VI. SUMMARY AND DISCUSSION

In this paper we have studied the quantum phases and phase transitions in the vicinity of the highly symmetric $SU(3)$ point in the spin-1 bilinear-biquadratic Heisenberg model on the square lattice by using a large-scale DMRG simulation. By computing spin and quadrupolar order parameters and correlation functions with tuning either the second-neighbor (K_2) or third-neighbor (K_3) biquadratic interaction, we established rich quantum phase diagrams with different spin dipolar and quadrupolar ordered phases. In addition, the nematic spin liquid phase which was reported recently near the $SU(3)$ model [22] was found to be robust in a wide parameter region varying the K_2, K_3 couplings. Furthermore, we calculated the nematic order parameters for different quantum phases. Nematic magnetic states break the lattice invariance under 90° rotations. We identified different lattice nematicity channels in the many quantum phases unveiled by using the B_{1g} and B_{2g} nematic orders. We also observed that the quantum phase transitions characterized by the nematic order parameters are consistent with those we find by spin and quadrupolar order parameters.

ACKNOWLEDGMENTS

We thank A. H. Nevidomskyy, H. Hu, R. Yu, and C. Batista for fruitful discussions. E.D. and W.-J.H. were supported by the US Department of Energy (DOE), Office of Science, Basic Energy Sciences (BES), Materials Science and Engineering Division. S.-S.G. was supported by NSFC Grants No. 11874078 and No. 11834014 and the Fundamental Research Funds for the Central Universities. H.-H.L. and Q.S. were supported by the US Department of Energy, Office of Science, Basic Energy Sciences, under Award No. DE-SC0018197 and Robert A. Welch Foundation under Grant No. C-1411. The majority of the computational calculations were performed on the Extreme Science and Engineering Discovery Environment (XSEDE) supported by NSF under Grant No. DMR160057. Most of the DMRG calculations were done by W.-J.H. and H.-H.L. at Rice University.

[1] K. Musaelian and R. Joynt, J. Phys.: Condens. Matter **8**, L105 (1996).
[2] L. Balents, Europhys. Lett. **33**, 291 (1996).
[3] M. Mulligan, C. Nayak, and S. Kachru, Phys. Rev. B **82**, 085102 (2010).
[4] M. Mulligan, C. Nayak, and S. Kachru, Phys. Rev. B **84**, 195124 (2011).
[5] J. Maciejko, B. Hsu, S. A. Kivelson, Y. J. Park, and S. L. Sondhi, Phys. Rev. B **88**, 125137 (2013).
[6] Y. Liu, S. Hasdemir, M. Shayegan, L. N. Pfeiffer, K. W. West, and K. W. Baldwin, Phys. Rev. B **88**, 035307 (2013).
[7] Y. You, G. Y. Cho, and E. Fradkin, Phys. Rev. X **4**, 041050 (2014).
[8] A. Gromov and D. T. Son, Phys. Rev. X **7**, 041032 (2017).
[9] L. Du, U. Wurstbauer, K. W. West, L. N. Pfeiffer, S. Fallahi, G. C. Gardner, M. J. Manfra, and A. Pinczuk, Sci. Adv. **5**, eaav3407 (2019).
[10] C. Fang, H. Yao, W.-F. Tsai, J. P. Hu, and S. A. Kivelson, Phys. Rev. B **77**, 224509 (2008).
[11] C. Xu, M. Müller, and S. Sachdev, Phys. Rev. B **78**, 020501(R) (2008).
[12] W. Bao, Y. Qiu, Q. Huang, M. A. Green, P. Zajdel, M. R. Fitzsimmons, M. Zhernenkov, S. Chang, M. Fang, B. Qian *et al.*, Phys. Rev. Lett. **102**, 247001 (2009).
[13] S. Li, C. de la Cruz, Q. Huang, Y. Chen, J. W. Lynn, J. Hu, Y.-L. Huang, F.-C. Hsu, K.-W. Yeh, M.-K. Wu *et al.*, Phys. Rev. B **79**, 054503 (2009).
[14] J. Dai, Q. Si, J.-X. Zhu, and E. Abrahams, Proc. Natl. Acad. Sci. USA **106**, 4118 (2009).
[15] J.-H. Chu, J. G. Analytis, K. De Greve, P. L. McMahon, Z. Islam, Y. Yamamoto, and I. R. Fisher, Science **329**, 824 (2010).
[16] P. Dai, J. Hu, and E. Dagotto, Nat. Phys. **8**, 709 (2012).
[17] S. Liang, A. Moreo, and E. Dagotto, Phys. Rev. Lett. **111**, 047004 (2013).

[18] R. M. Fernandes, A. V. Chubukov, and J. Schmalian, Nat. Phys. **10**, 97 (2014).
[19] X. Lu, J. T. Park, R. Zhang, H. Luo, A. H. Nevidomskyy, Q. Si, and P. Dai, Science **345**, 657 (2014).
[20] C. B. Bishop, A. Moreo, and E. Dagotto, Phys. Rev. Lett. **117**, 117201 (2016).
[21] C. B. Bishop, J. Herbrych, E. Dagotto, and A. Moreo, Phys. Rev. B **96**, 035144 (2017).
[22] W.-J. Hu, S.-S. Gong, H.-H. Lai, H. Hu, Q. Si, and A. H. Nevidomskyy, Phys. Rev. B **100**, 165142 (2019).
[23] N. Papanicolaou, Nucl. Phys. B **305**, 367 (1988).
[24] S. Nakatsuji, Y. Nambu, H. Tonomura, O. Sakai, S. Jonas, C. Broholm, H. Tsunetsugu, Y. Qiu, and Y. Maeno, Science **309**, 1697 (2005).
[25] J. G. Cheng, G. Li, L. Balicas, J. S. Zhou, J. B. Goodenough, C. Xu, and H. D. Zhou, Phys. Rev. Lett. **107**, 197204 (2011).
[26] B. Fåk, S. Bieri, E. Canévet, L. Messio, C. Payen, M. Viaud, C. Guillot-Deudon, C. Darie, J. Ollivier, and P. Mendels, Phys. Rev. B **95**, 060402(R) (2017).
[27] J. A. Quilliam, F. Bert, A. Manseau, C. Darie, C. Guillot-Deudon, C. Payen, C. Baines, A. Amato, and P. Mendels, Phys. Rev. B **93**, 214432 (2016).
[28] R. Yu, Z. Wang, P. Goswami, A. H. Nevidomskyy, Q. Si, and E. Abrahams, Phys. Rev. B **86**, 085148 (2012).
[29] R. Yu and Q. Si, Phys. Rev. Lett. **115**, 116401 (2015).
[30] Z. Wang, W.-J. Hu, and A. H. Nevidomskyy, Phys. Rev. Lett. **116**, 247203 (2016).
[31] S.-S. Gong, W. Zhu, D. N. Sheng, and K. Yang, Phys. Rev. B **95**, 205132 (2017).
[32] H.-H. Lai, W.-J. Hu, E. M. Nica, R. Yu, and Q. Si, Phys. Rev. Lett. **118**, 176401 (2017).
[33] F. D. M. Haldane, Phys. Rev. Lett. **50**, 1153 (1983).
[34] I. Affleck, T. Kennedy, E. H. Lieb, and H. Tasaki, Phys. Rev. Lett. **59**, 799 (1987).
[35] K. Katsumata, H. Hori, T. Takeuchi, M. Date, A. Yamagishi, and J. P. Renard, Phys. Rev. Lett. **63**, 86 (1989).
[36] M. Hagiwara, K. Katsumata, I. Affleck, B. I. Halperin, and J. P. Renard, Phys. Rev. Lett. **65**, 3181 (1990).
[37] S. R. White and D. A. Huse, Phys. Rev. B **48**, 3844 (1993).
[38] U. Schollwöck, T. Jolicœur, and T. Garel, Phys. Rev. B **53**, 3304 (1996).
[39] D. G. Shelton, A. A. Nersesyan, and A. M. Tsvelik, Phys. Rev. B **53**, 8521 (1996).
[40] A. Läuchli, G. Schmid, and S. Trebst, Phys. Rev. B **74**, 144426 (2006).
[41] P. Corboz, A. M. Läuchli, K. Totsuka, and H. Tsunetsugu, Phys. Rev. B **76**, 220404(R) (2007).
[42] I. Niesen and P. Corboz, Phys. Rev. B **95**, 180404(R) (2017).
[43] F. Haldane, Phys. Lett. A **93**, 464 (1983).
[44] E. Lieb, T. Schultz, and D. Mattis, Ann. Phys. (NY) **16**, 407 (1961).
[45] M. B. Hastings, Phys. Rev. B **69**, 104431 (2004).
[46] H. J. Changlani and A. M. Läuchli, Phys. Rev. B **91**, 100407(R) (2015).
[47] A. Läuchli, F. Mila, and K. Penc, Phys. Rev. Lett. **97**, 087205 (2006).
[48] T. A. Tóth, A. M. Läuchli, F. Mila, and K. Penc, Phys. Rev. Lett. **105**, 265301 (2010).
[49] T. A. Tóth, A. M. Läuchli, F. Mila, and K. Penc, Phys. Rev. B **85**, 140403(R) (2012).
[50] B. Bauer, P. Corboz, A. M. Läuchli, L. Messio, K. Penc, M. Troyer, and F. Mila, Phys. Rev. B **85**, 125116 (2012).
[51] H. H. Zhao, C. Xu, Q. N. Chen, Z. C. Wei, M. P. Qin, G. M. Zhang, and T. Xiang, Phys. Rev. B **85**, 134416 (2012).
[52] P. Corboz, K. Penc, F. Mila, and A. M. Läuchli, Phys. Rev. B **86**, 041106(R) (2012).
[53] P. Corboz, M. Lajkó, K. Penc, F. Mila, and A. M. Läuchli, Phys. Rev. B **87**, 195113 (2013).
[54] I. Niesen and P. Corboz, SciPost Phys. **3**, 030 (2017).
[55] I. Niesen and P. Corboz, Phys. Rev. B **97**, 245146 (2018).
[56] Y. Wang, W. Hu, R. Yu, and Q. Si, Phys. Rev. B **100**, 100502(R) (2019).
[57] S. R. White, Phys. Rev. Lett. **69**, 2863 (1992).
[58] I. McCulloch and M. Gulácsi, Europhys. Lett. **57**, 852 (2002).
[59] M. Blume and Y. Hsieh, J. Appl. Phys. **40**, 1249 (1969).
[60] P. Chandra, P. Coleman, and A. I. Larkin, Phys. Rev. Lett. **64**, 88 (1990).